Available online at www.sciencedirect.com
ScienceDirect
Mathematics and Computers in Simulation 190 (2021) 1392–1414
MATHEMATICS AND COMPUTERS IN SIMULATION
www.elsevier.com/locate/matcom

Original articles

Benchmarking the geometrical robustness of a Virtual Element Poisson solver

Marco Attene, Silvia Biasotti, Silvia Bertoluzza, Daniela Cabiddu*, Marco Livesu, Giuseppe Patanè, Micol Pennacchio, Daniele Prada, Michela Spagnuolo

Istituto di Matematica Applicata e Tecnologie Informatiche "E. Magenes", CNR, Italy

Received 19 December 2020; received in revised form 31 May 2021; accepted 19 July 2021
Available online 29 July 2021

Abstract

Polytopal Element Methods (PEM) allow us solving differential equations on general polygonal and polyhedral grids, potentially offering great flexibility to mesh generation algorithms. Differently from classical finite element methods, where the relation between the geometric properties of the mesh and the performances of the solver are well known, the characterization of a good polytopal element is still subject to ongoing research. Current shape regularity criteria are quite restrictive, and greatly limit the set of valid meshes. Nevertheless, numerical experiments revealed that PEM solvers can perform well on meshes that are far outside the strict boundaries imposed by the current theory, suggesting that the real capabilities of these methods are much higher. In this work, we propose a benchmark to study the correlation between general 2D polygonal meshes and PEM solvers which we test on a virtual element solver for the Poisson equation. The benchmark aims to explore the space of 2D polygonal meshes and polygonal quality metrics, in order to understand if and how shape regularity, defined according to different criteria, affects the performance of the method. The proposed tool is quite general, and can be potentially used to study any PEM solver. Besides discussing the basics of the benchmark, we demonstrate its application on a representative member of the PEM family, namely the Virtual Element Method, also discussing our findings.

Keywords: Polytopal Element Methods; Virtual Element Methods; Polygonal meshes; Geometric metrics; Geometry-PEM correlation

1. Introduction

Solving a PDE on geometrically complex domains is a fundamental task, frequently encountered in scientific computing. In real applications, the generation of a good discretization of the input domain is a key aspect to obtain quality results, but it can also be an extremely complex problem, often even harder than the numerical solution of the discretized equations [16]. To alleviate meshing issues, recent literature suggests to resort to Polytopal Element Methods (PEM), i.e., methods for the numerical solution of PDEs based on polygonal and polyhedral grids. PEM approaches allow us to: (i) achieve high flexibility in the treatment of complex geometries; (ii) incorporate complex features at different scales without triggering mesh refinement; (iii) automatically include hanging nodes (i.e., T-junctions); and (iv) simplify refinement and coarsening operators. Main PEMs include Mimetic Finite

* Corresponding author.
E-mail address: daniela.cabiddu@cnr.it (D. Cabiddu).

https://doi.org/10.1016/j.matcom.2021.07.018

Differences [3,37], Discontinuous Galerkin-Finite Element Method (DG-FEM) [1,4], Hybridizable and Hybrid High-Order Methods [6,24], Weak Galerkin Method [39], BEM-based FEM [25], Poly-Spline FEM [26], and Polygonal FEM [32]. As a representative example of the PEM family of approaches, we consider the *Virtual Element Method* (VEM) [34], which can be considered as an extension to FEM for handling general polytopal meshes.

Similarly to standard finite elements, the performance of PEM depends on the quality of the underlying mesh, in terms of accuracy, stability, and overall computational cost. On the other hand, while the concept of shape regularity of triangular/tetrahedral and quadrangular/hexahedral meshes is well understood [2,5,29], the characterization of a good polytopal mesh is still subject to ongoing research. Unlike classical finite elements, the enormous freedom in terms of different shapes given by the polytopal framework, makes it difficult to identify exactly which geometric features do or do not have a negative effect on the performance of the method. Recent works on shape regularity for PEM [19,22], see also [13], assume each element in the mesh to be star-shaped with respect to all points in a circle of diameter comparable with the diameter of the elements itself. Moreover, it is often assumed that the length of all edges is also comparable with the element diameter. In particular, the analysis of the VEM often connects the approximation error with the ratio between the radius of the circumscribed circle and the radius of the circle inscribed in the kernel of the element. Moreover, the optimality of the method is only achieved in an even stricter framework (see Assumption A.2 in Appendix A). However, numerous numerical tests seem to indicate that PEMs allow to reliably solve PDEs even on apparently very "bad" meshes, violating one or more of such conditions. Such results suggest that there is a gap between the current theory and the real capabilities of the solver, thus allowing much weaker requirements on the tessellation that still guarantee the convergence of PEM solvers.

The issue of assessing the capabilities of a numerical method when paired with a particular mesh has recently been considered also by the geometry processing community, where solutions of differential equations have been extensively used for a variety of applications, such as mesh parameterization [10], computation of diffusion distances [23], Voronoi diagrams [15], and smoothing [7,21]. In [12], the FEM performances on hexahedral meshes have been analyzed on meshes with various geometric metrics [31]. Schneider et al. [27] identify in mesh resolution, element quality, and basis order the three factors that affect the accuracy of standard FEM, and advocate the use of higher order basis to compensate badly shaped elements. A similar analysis for the PEM case, is far from trivial as: (i) there are no available resources in terms of mesh databases, and (ii) no consensus has yet been reached on what are the right metrics to consider to evaluate the mesh quality with respect to the performances of the solver.

In this paper we introduce a computational framework and a tool, for the analysis of the correlation between the performance of a given PEM solver and a wide set of polygon quality metrics, aimed at systematically exploring the relation between the geometric properties of the mesh and the performances of the PEM solver (Section 2). The final goal is to identify: (i) more permissive shape-regularity criteria under which the considered method is effective, and (ii) specific issues that negatively affect the results, in order to support the design of better polygonal meshing methods.

To this end, we consider 14 geometric properties of polygons (Table 1), spanning from areas, angles, and edge length, to kernels, inscribed and circumscribed circles, which, via different aggregation strategies (minima, maxima, averages, worst case scenario and Euclidean norm) yield 60 per mesh metrics. Concerning polygonal meshes, the available Voronoi-based meshing tools (e.g. [9]) are not the best suited for our study, as they produce convex elements that – we believe – are not challenging enough to put PEM solvers to test. Instead, we opt for a family of parametric elements designed to progressively stress one or more of the proposed geometric metrics, enriched with random polygons in order to avoid a bias in the study. For the analysis of the performance of the PEM solver, we consider different "performance indices", including the accuracy of the solution and the conditioning of the associated linear system. Finally, while we consider here the Virtual Element Method, the whole framework can be applied to any PEM method, and is highly modular, thus favoring further extensions with new polygons, metrics and/or performance indices (Section 3).

While previous works [13,19,22] address the concept of shape quality metrics and study its effect on the different quantities directly involved in the analysis of polytopal approximation estimates, such as the Poincaré constant, or the constant appearing in inverse inequalities, at an elemental level, to the best of our knowledge (Section 4), this work is the first attempt at systematically studying the correlation between polygonal numerical methods to solve PDEs and different possible definitions of quality metrics for the whole underlying polygonal tessellation. Of course, the benchmark can be used, with the same strategy, to analyze other polytopal methods. We believe the results of such an analysis will provide useful input to two communities. For the geometry processing community, metrics with a

Table 1
List of the proposed polygonal quality metrics.

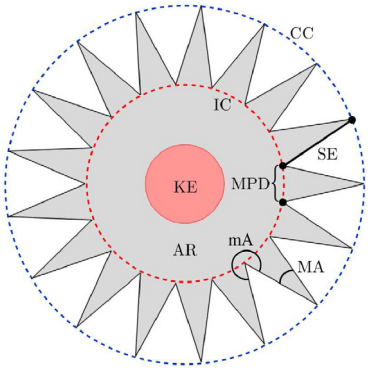

Metric	Abbr.	Range	Scale inv.
Circumscr. radius	CC	$(0,\infty)$	No
Inscr. radius	IC	$(0,\infty)$	No
Circle ratio	CR	$[0,1]$	Yes
Area	AR	$[0,\infty)$	No
Kernel-area	KE	$[0,\infty)$	No
Kernal-area ratio	KAR	$[0,1]$	Yes
Area-perim.^{2} ratio	APR	$(0,1]$	Yes
Shortest edge	SE	$(0,\infty)$	No
Scaled shortest edge	sSE	$(0,\sqrt{3})$	Yes
Edge ratio	ER	$(0,1]$	Yes
Min p2p dist.	MPD	$(0,\infty)$	No
Scaled Min p2p dist.	sMPD	$(0,\sqrt{3})$	Yes
Min. angle	MA	$(0,\pi)$	Yes
Max. angle	MX	$(0,2\pi)$	Yes
♯ Edges	nE	$(1,+\infty)$	Yes
Shape reg.	SR	$[0,1)$	Yes
Isotropy	ISO	$(0,1)$	Yes

good correlation with the solver could be incorporated into meshing tools in order to generate polygonal grids and refinement/coarsening operators that fully exploit the flexibility granted by PEM, thus supporting the development of new PDE-aware mesh processing tools. For the math community, correlations will suggest directions to further improve the theory, developing more permissive shape-regularity criteria for the current methods, and new methods to overcome the limitations of the current solvers.

2. Benchmark

We present a benchmark that allows us to investigate the correlation of a set of polygonal quality measures (Section 2.1) with the performance indices for a PEM solver (Section 3.1). The relation between these entities is assessed on a carefully crafted set of discrete polygonal meshes (Section 2.2). Our approach is quite general, and it can be used to potentially evaluate any PEM solver. To this end, the solver itself is not part of the benchmark, but is treated as an external black box, taking in input a mesh , and returning the solution of a PDE (Fig. 2). The output of the benchmark is a set of geometric measures related to the mesh itself and a set of performance parameters related to the PDE solver, which are computed on the meshes described in Section 2.2.

2.1. Polygonal quality metrics

For the geometric part, we include in the benchmark a set of polygonal metrics (Table 1), stressing out different characteristics, related to the size and shape of the elements. More precisely, we consider the following parameters.

1. *Circumscribed circle radius (CC)*: the radius of the smallest circle fully containing P. We compute CC by treating the vertices of P as a point cloud and running the Welzl's algorithm to solve the minimum covering circle problem [41]. Remark that our definition differs from the circumcircle of a polygon that corresponds to the circle that passes through all the vertices of the polygon and does not necessarily exist for all polygons (Fig. 3);
2. *inscribed circle radius (IC)*: the radius of the biggest circle fully contained in P. For its computation, we start from a Voronoi diagram of the edges of P, and select the corner in the diagram that is furthest from all edges as center of the circle. The minimum distance between such point and any of the edges of P is

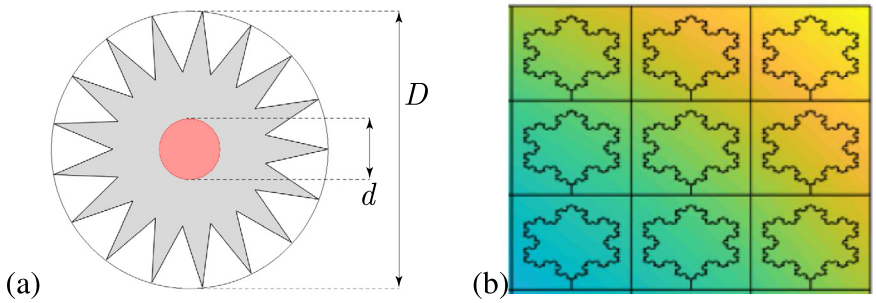

Fig. 1. (a) Minimal polygon shape regularity expressed in terms of the ratio between the maximal ball inscribed in the kernel of the polygon (d), and the maximal ball inscribing the element (D). (b) Polygonal mesh composed of snowflake-like elements and their dual, which violate any known shape regularity criterion for polygonal elements.

the radius of the IC. Differently from the point case, the diagram of a set of segments has curved boundaries between cells; for its computation, we rely on the Boost Polygon Library [30];

3. *circle ratio (CR)*: the ratio between IC and CC. Differently from the previous two, this measure does not depend on the scale of the polygon, and is always defined in the range (0, 1];
4. *area (AR)*: the area of the polygon P;
5. *kernel area (KE)*: the area of the kernel of the polygon, defined as the set of points $p \in P$ from which the whole polygon is visible. If the polygon is convex, then the area of the polygon and the area of the kernel are equal. If the polygon is star-shaped, then the area of the kernel is a positive number. If the kernel is non star-shaped, then the polygon has no kernel and KE will be zero;
6. *kernel-area ratio (KAR)*: the ratio between the area of the kernel of P and its whole area. For convex polygons, this ratio is always 1. For concave star-shaped polygons, KAR is strictly defined in between 0 and 1. For non star-shaped polygons, KAR is always zero;
7. *area–perimeter squared ratio (APR)*, or *compactness*: defined as $\frac{2\pi * \text{area}(P)}{\text{perimeter}(P)^2}$. This measure reaches its maximum for the most compact 2D shape (the circle), and becomes smaller for less compact polygons;
8. *shortest edge (SE)*: the length of the shortest edge of P;
9. *scaled shortest edge (sSE)*: the ratio between the length of the shortest edge and the circumscribed circle radius.
10. *edge ratio (ER)*: the ratio between the length of the shortest and the longest edge of P;
11. *minimum point to point distance (MPD)*, which is the minimum distance between any two vertexes in P. In case the two vertex points in P are also consecutive, MPD and SE are equivalent;
12. *scaled minimum point to point distance (sMPD)*, which is the ratio between the minimum distance between any two vertexes in P, and the radius of the circumscribed circle;
13. *minimum angle (MA)*: the minimum inner angle of the polygon P;
14. *maximum angle (MX)*: the maximum inner angle of the polygon P;
15. *number of edges (nE)*: the number of edges of the input polygonal mesh;
16. *shape regularity (SR)*: the ratio between the radius of the circle inscribed in the kernel of the element and the radius of the circle circumscribed to the element (see Fig. 1).
17. *isotropy (ISO)*: this is the ratio between the minimum and the maximum eigenvalue of the covariance matrix M_{Cov} relative to the polygon K, which is defined as

$$M_{\text{Cov}} = \frac{1}{|K|} \int_K (x - \bar{x}_K)^T (x - \bar{x}_K),$$

$|K|$ denoting the area of the polygon K and $\bar{x}_K$ its baricenter. The quotient of the two eigenvalue characterized the anisotropy of the polygon [40]: if close to 1, the polygon is isotropic, if $\ll 1$ the polygon is anisotropic.

2.2. Polygonal meshes

To evaluate the dependence of the performance of a PEM solver on the geometrical features of the underlying mesh, we propose a set of polygonal meshes explicitly designed to progressively stress the proposed metrics.

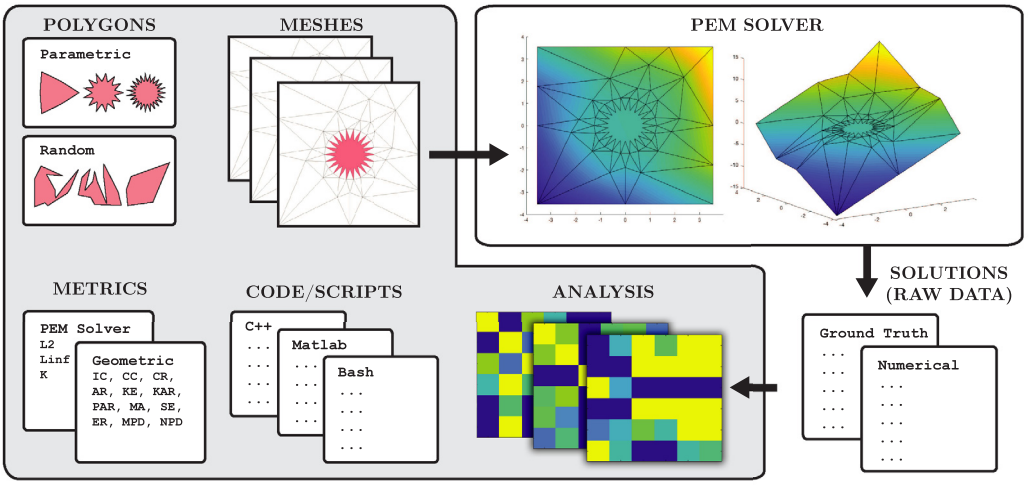

Fig. 2. Proposed benchmark (gray shaded area) and its relation with the PEM solver. The benchmark is composed of a set of both parametric and random polygons and a set of tools (C++/Matlab code and Bash scripts) to perform mesh generation, geometric qualities and PEM performances computation, and correlation analysis. To be quite general, the PEM solver is not included in our benchmark.

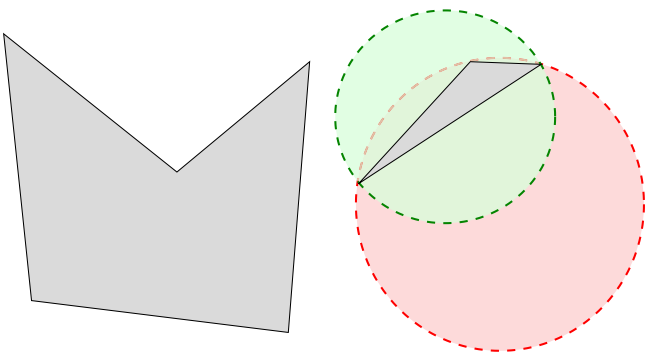

Fig. 3. (Left) Polygon that does not admit a circumscribed circle. To be able to scale on general polygons, we define the radius of the circumscribed circle (CC) as the radius of the smallest circle containing the polygon itself. (Right) For a strongly anisotropic skinny triangle, CC is the radius of the smallest circle that passes through the endpoints of its longest edge (green), and not of the circle passing through all its three vertices (red). (For interpretation of the references to color in this figure legend, the reader is referred to the web version of this article.)

We achieve this goal by generating a family of parametric polygons, $P(t)$, with $t \in [0, 1]$. Each polygon has a benign baseline configuration ($P(0)$), and is progressively subject to a deformation, controlled by the parameter t. The baseline configuration has no or little critical geometrical features and it satisfies a strong shape regularity assumption which is standard in the analysis of PEM solvers, namely, it is the union of a small number of shape regular triangles. The deformations are designed in such a way that such an assumption is progressively violated in different ways.

More precisely, we designed 8 different parametric polygons; for each polygon, we show, in Fig. 4, its evolution for growing values of t, and we report the geometric metrics it affects (Table 2). To minimize any bias due to artificially constructed polygons, we enrich the family of elements with randomly generated polygons (Fig. 5), created with CGAL [33]. We used Cinolib [20] for polygon mesh processing and metric measurements.

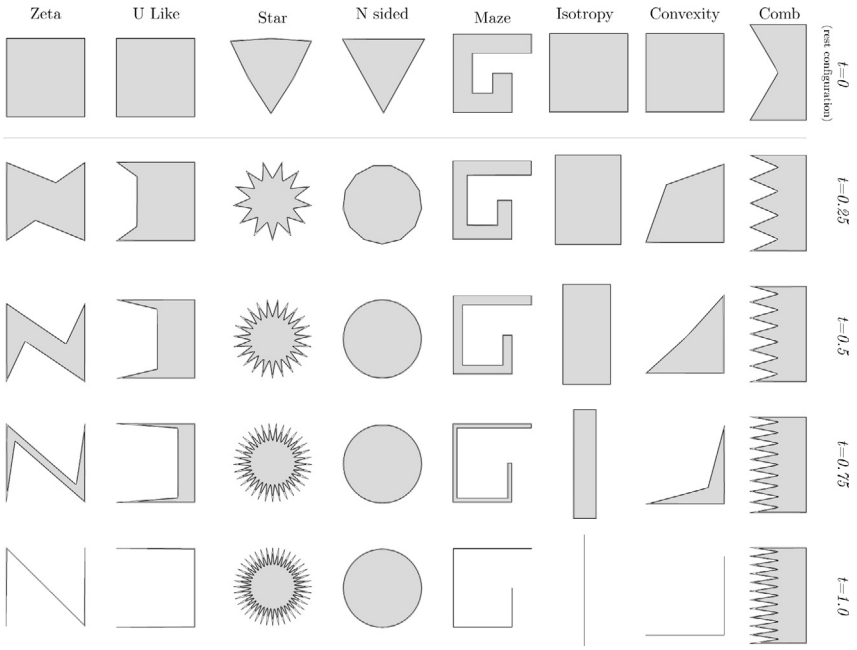

Fig. 4. The eight families of parametric polygons that generate the meshes in the dataset. Each polygon starts from a rest configuration ($t = 0$, top row) and progressively degenerates by increasing t, thus stressing either one or multiple quality measures in Table 1.

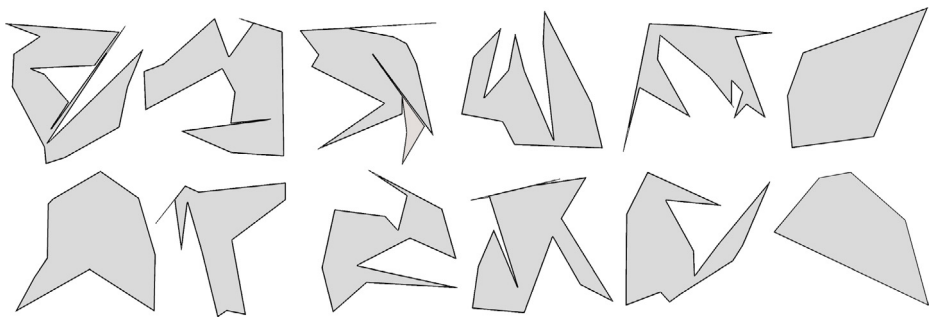

Fig. 5. Examples of random polygons in our benchmark, with a large variety in terms of complexity of the shapes, spanning from simple convex polygons (top right) to extremely challenging ones (top left).

Given both the parametric and random polygons, the 2D polygonal meshes for the domain $[0, 1]^2$ are created by placing an element at the center of a squared canvas, and filling the rest of the domain with triangles, using [28]. Since we are interested in the response of the PEM solver with respect to the parametric and random polygons, we fill the rest of the domain with well shaped elements by imposing that 20° is the minimum inner angle for each triangle. Note that quality bounds are not guaranteed for triangles incident to constrained edges, therefore the angle threshold may be violated by elements incident to our test polygons, which can be arbitrarily badly shaped. To complete our analysis, we also create a sequence of progressively finer grids, obtained by mirroring the squared domains multiple times (Fig. 6).

Evaluating each of the above quality metrics on all the elements of a given mesh yields a real valued vector whose length is the number of elements. In order to derive a single valued quality metric for the mesh out of the vector

Table 2
Correlation between geometric metrics and parametric polygons.

	Comb	Convexity	Isotropy	Maze	N Sided	Star	U Like	Zeta
CC			✓		✓			
IC	✓	✓	✓	✓	✓		✓	✓
CR	✓	✓	✓	✓			✓	✓
AR	✓	✓	✓	✓		✓	✓	✓
KE		✓	✓				✓	✓
KAR		✓	✓			✓	✓	✓
APR	✓			✓			✓	✓
SE			✓	✓	✓			
ER			✓	✓				
MPD	✓	✓	✓	✓	✓	✓	✓	✓
MA	✓	✓		✓		✓	✓	✓
MX	✓	✓				✓	✓	✓
nE	✓	✓	✓	✓			✓	✓
SR	✓	✓	✓	✓	✓	✓	✓	✓

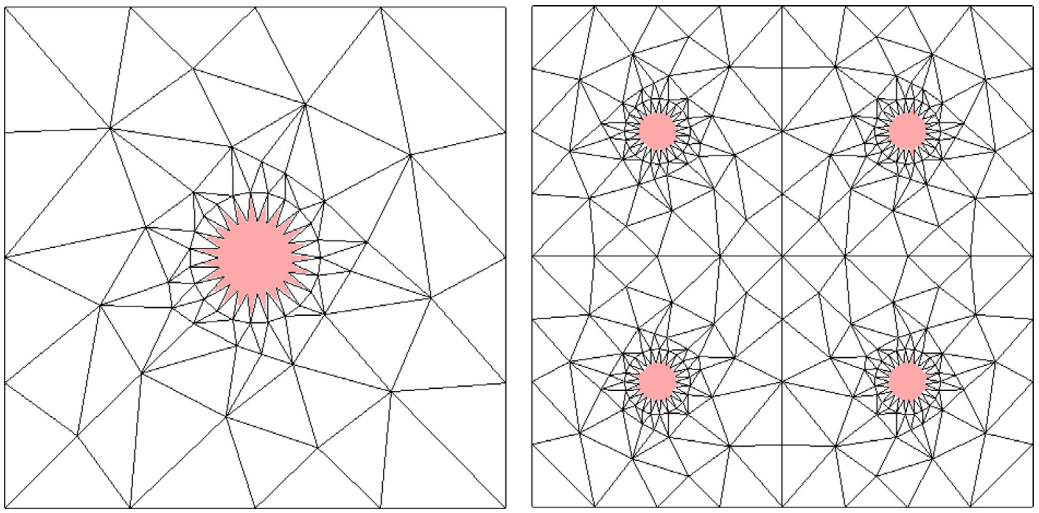

Fig. 6. (Left) Example of a 2D polygonal mesh in the benchmark. (Right) A mesh hierarchy is also obtained by mirroring the meshes, thus reducing the average edge length and enabling convergence checks.

of elemental quality metrics, we can consider several recipes, which we will refer to as "aggregation strategies" or "aggregation methods". We can take the mean, geometric mean, euclidean norm, maximum, minimum and worst, where, depending on the measure, worst is chosen to be the most significant between minimum and maximum.

3. Benchmarking the virtual element method

We now use the benchmark for a preliminary study of the robustness, with respect to different geometric features of the mesh, of a specific PEM solver for the solution of the Poisson equation on the unit square $\Omega =]0, 1[^2$:

Problem 3.1. Given sufficiently smooth functions $f : \Omega = (0, 1)^2 \to \mathbb{R}$ and $g : \partial\Omega \to \mathbb{R}$, find u solution to

$$-\Delta u = -\frac{\partial^2 u}{\partial x^2} - \frac{\partial^2 u}{\partial y^2} = f, \text{ in } \Omega, \qquad u = g \text{ on } \partial\Omega.$$

More specifically, we will consider the *virtual element method* Appendix A.

3.1. Performance metrics of the VEM PEM solver

Considering the exact ground-truth solution u and the approximated solution u_h computed with a PEM solver (in our case, the VEM), and letting S denote the stiffness matrix stemming from the method, we consider the following parameters, which we refer to as "performance index" (or "performance metrics").

- *relative error in the discrete energy norm*:

$$\epsilon_S := \frac{\|u - u_h\|_S}{\|u\|_S},$$

  where the discrete energy norm $\|v_h\|_S$ – equivalent to the $H^1([0,1]^2)$ norm – is defined in Appendix A;
- *polynomial component of the relative discrete energy error*:

$$\epsilon_\pi := \|\Pi^\nabla(u - u_h)\|_S / \|u\|_S,$$

  where the discrete projector Π^∇ onto the space of discontinuous piecewise polynomials of order k is defined in Appendix A;
- *relative $\mathcal{L}_\infty$-error*:

$$\epsilon_\infty := \|u - u_h\|_\infty / \|u\|_\infty, \quad \text{where } \|v\|_\infty = \max_{\mathbf{x}\in\Omega} v(\mathbf{x}).$$

- *relative $\mathcal{L}_2$-error*

$$\epsilon_0 := \|u - u_h\|_0 / \|u\|_0, \quad \text{where } \|v\|_0 = \left(\int_\Omega v(\mathbf{x})^2 \, d\mathbf{x}\right)^{1/2}.$$

We also consider some quantities related to the stiffness matrix stemming from the discretization, namely:

- *$\mathcal{L}_2$ condition number of the stiffness matrix*:

$$\kappa_2(S) = \|S\|_2 \|S^{-1}\|_2,$$

  where, with an abuse of notation, for a matrix S we indicate by $\|S\|_2$ the matrix norm induced by the Euclidean vector norm. The condition number measures the cost of solving, by an iterative solver, the linear system stemming from the method, and also represents an indicator of the numerical stability of said linear system. For very high condition numbers, the effect of roundoff errors might strongly affect the computed discrete solution, making it unreliable, despite the validity of an priori error estimate of the form (1); indeed, even if we neglect the roundoff errors arising in the computation of the stiffness matrix and in the solution of the linear system, but only consider the effect of the error deriving from round off in the computation of the right hand side, this is amplified, when measured in the euclidean norm, by a factor $\|S^{-1}\|_2$ which, for very high condition number, is itself very high.
- *$\mathcal{L}_2$ condition number of the stiffness matrix, after preconditioning*:

$$\kappa_2(P^{-1}S) = \|P^{-1}S\|_2 \|(P^{-1}S)^{-1}\|_2,$$

  where $P = KK^T$, with K sparse approximation to L, lower triangular matrix such that $S = LL^T$, is the Incomplete Choleski preconditioner [14] (in our numerical tests we used the Matlab function `ichol` with the default value for all the parameters); if the incomplete Choleski decomposition algorithm fails, P is set equal to the identity matrix, and $\kappa_2(P^{-1}S) = \kappa_2(S)$;

The six above performance indicators a priori depend both on the size and the shape of the elements of the mesh, and will be referred to as *unscaled* performance indices.

As we are here rather interested in studying the effect of the element shape on the performance of the method, than in studying its dependence on their size, we also added a number of *scaled* performance indices, which we expect to be independent of the mesh size. More precisely, we consider the value of the constants appearing in some classical inequalities relating, a priori, the error in the solution to the element size. The first scaled indicator is the constant in the classical a priori error estimate, valid for order k methods (see (A.4)), of the form

$$\|u - u_h\|_1 \lesssim h^k \|u\|_{k+1}, \tag{1}$$

where for $k \geq 1$ integer,

$$\|v\|_k = \left(\sum_{|\alpha| \leq k} \int_\Omega |\partial^\alpha v|^2 \right)^{1/2}$$

denotes the standard norm for the Sobolev space $H^k(\Omega)$. The second scaled index is the constant in the a priori estimate for the L^2 norm of the form

$$\|u - u_h\|_0 \lesssim h \|u - u_h\|_1, \tag{2}$$

which can be obtained via an Aubin–Nitsche type duality arguments. While such estimates are usually proven with h denoting the maximum of the element diameters ($h = CC_{\max}$), motivated by the results obtained in Section 3.4, we rather consider here the constant appearing in such inequalities, when setting $h = CC_{\text{av}}$. More precisely we consider the following additional performance metrics

- *Scaled discrete energy norm error*
$$C_{\text{S}}^{\text{err}} = \frac{\epsilon_S}{h^k}, \qquad h = CC_{\text{av}}$$
- *Scaled discrete energy norm error — polynomial component*
$$C_{\pi}^{\text{err}} = \frac{\epsilon_\pi}{h^{k+1}}, \qquad h = CC_{\text{av}}$$
- *Scaled L^2 error*
$$C_{0}^{\text{err}} = \frac{\epsilon_0}{h^{k+1}}, \qquad h = CC_{\text{av}}$$
- *Scaled L^∞ error*
$$C_{\infty}^{\text{err}} = \frac{\epsilon_i nf}{h^{k+1}}, \qquad h = CC_{\text{av}}$$
- *Aubin–Nitsche constant*:
$$C_{\text{AN}} = \frac{\epsilon_2}{h\epsilon_S}, \qquad h = CC_{\text{av}}$$

Finally, we consider a scaled performance indicator relative to the conditioning of the linear system stemming from the method, and, more precisely, we measure the following quantity.

- *effectiveness of the incomplete Choleski (IC) preconditioner*: the ratio
$$\kappa_2(P^{-1}S)/\kappa_2(S),$$
measuring the improvement in the condition number deriving from applying the IC preconditioner.

3.2. Test — polygonal dataset

For each one of the eight base polygons, we pick 20 equally spaced samples in their parameter domain [0, 1], thus producing 160 different polygons, classified in eight families. We complement this set with 100 *random* meshes. Each of these polygons is applied to generate a mesh for the unit square (Section 2.2) and the resulting 160 meshes constitute our dataset D_0. Furthermore, the domain *mirroring* (Section 2.2) is applied to generate two refined versions (D_1, D_2) of D_0. Each dataset D_i has four times more polygons than D_{i-1}, and the same ratio between number of triangles and generic polygons. In Table 3 we report the value of mean and standard deviation (StD) for the fourteen metrics at hand, with the two aggregation methods "Average" and "Worst", on the dataset D_0.

3.3. Poisson equation: test cases

To assess the geometrical robustness of the method, we consider three test cases, corresponding to three different right hand sides and Dirichlet data for the Poisson equation. In Fig. 7 we display the three corresponding exact solutions.

Table 3
Statistical information on the polygonal meshed dataset D0, for the metrics considered and the average and worst aggregation methods.

	Average		Worst	
	Mean	StD	Mean	StD
CC	0.12472	0.028738	0.057496	0.042099
IC	0.051734	0.012359	0.019356	0.015859
AR	0.01815	0.0057874	0.0048612	0.0059034
KE	0.017819	0.0057906	0.0031064	0.0054629
SE	0.16506	0.043433	0.070566	0.062979
MPD	0.16465	0.043168	0.05771	0.05491
CR	0.41584	0.020346	0.1797	0.067243
KAR	0.98879	0.0082072	0.31767	0.43328
APR	0.041968	0.001603	0.051721	0.0083875
sSE	1.3040	0.0949	0.4665	0.3376
sMPD	1.3017	0.0934	0.3377	0.3111
ER	0.68067	0.054774	0.29407	0.17503
SR	0.4133	0.0204	0.0938	0.1024
MA	0.72101	0.060885	0.27895	0.13256
MX	1.4875	0.05341	4.4689	1.3387
NS	3.1578	0.1201	15.9462	15.3416
ISO	0.4129	0.0651	0.0616	0.0248

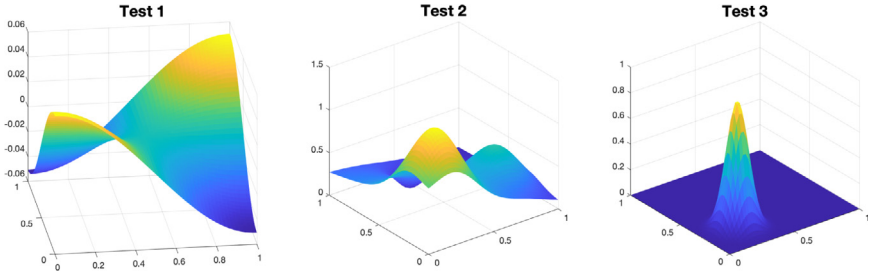

Fig. 7. Exact solution for test cases 1, 2 and 3.

Test case 1 (trigonometric solution)

The Dirichlet boundary condition g and the load term f are taken in such a way that

$$u(x, y) := \frac{\cos(\pi x)\cos(\pi y)}{2\pi^2}$$

is the exact solution.

Test case 2 (franke function)

The Dirichlet boundary condition g and the load term f are taken in such a way that the Franke function [11]

$$u(x, y) := \frac{3}{4}e^{-\left((9x-2)^2+(9y-2)^2\right)/4} + \frac{3}{4}e^{-\left((9x+1)^2/49+(9y+1)/10\right)} + \frac{1}{2}e^{-\left((9x-7)^2+(9y-3)^2\right)/4} + \frac{1}{5}e^{-\left((9x-4)^2+(9y-7)^2\right)}$$

is the exact solution.

Test case 3 (gaussian function)

The Dirichlet boundary condition g and the load term f are taken in such a way that the solution is the gaussian function

$$u(x, y) = e^{-100(x-.25)^2+(y-.25)^2}.$$

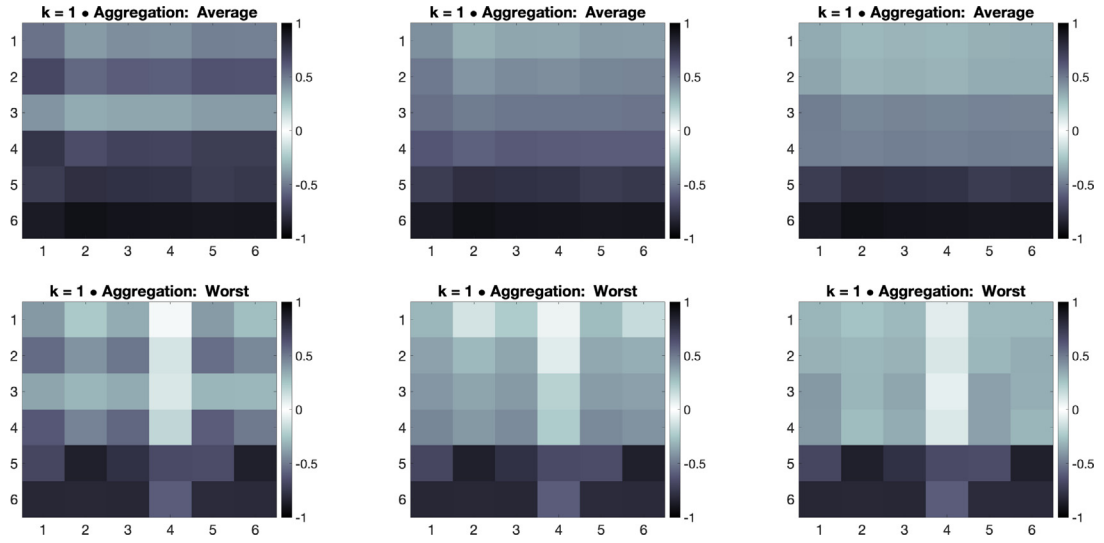

Fig. 8. Unscaled mesh metrics (average aggregation strategy (top) and worst aggregation strategy (bottom) vs unscaled performance metrics for order $k = 1$, Test cases 1, 2 and 3 (left to right). Metrics (horizontal axis): CC (1), IC (2), AR (3), KE (4), SE (5), MPD (6) – Performances (vertical axis): energy error (1), energy error — polynomial component (2), L^∞ error (3), L^2 error (3), stiffness matrix condition number (5), preconditioner stiffness matrix condition number (6). For the pixel (i, j) the corresponding gray level represents the absolute value of the correlation between the ith performance index and the jth metric. Dark values represent high positive or negative correlation, light value represents low correlation. (For interpretation of the references to color in this figure legend, the reader is referred to the web version of this article.)

3.4. Determination of the global mesh size parameter

In order to choose which aggregation method to use in order to define, for each mesh, a single mesh size parameter, we evaluate the correlation between the different scale dependent metrics (namely CC,) and the scale dependent performances. We focus on two aggregation methods (average and worst), the euclidean norm and geometric mean aggregation method give similar results as the average aggregation method, and the worst element value aggregation method summarizes the remaining two (max and min).

More precisely, for the method of order $k = 1$ and the three test cases, we compute the Spearman correlation index between the 6 scale dependent geometric metrics and the 6 unscaled performance indices. As in our case the distribution of the concerned variables is not normal (this property is ascertained by resorting to the Kolmogorov–Smirnov test [8]), here, and in all the subsequent tests, we evaluated the correlation by using the Spearman rank correlation index ρ_S [8]. This is defined as

$$\rho_S(X, Y) = \frac{\mathrm{cov}(\mathrm{rg}_X, \mathrm{rg}_Y)}{\sigma_{\mathrm{rg}_X} \sigma_{\mathrm{rg}_Y}},$$

where $\mathrm{cov}(x, y)$ denotes the covariance of the two variable x and y, σ_x denotes the standard deviation of the variable x, and where rg_x denotes the ranking of the variable x, defined as the variable obtained from x by replacing each value with its ranking when the data are sorted. The absolute value of the correlations is displayed in Fig. 8 in a gray level scale: the level of gray of the pixel (i, j) represents the absolute value of the correlation between the ith unscaled performance and the j unscaled metrics (dark pixels correspond to high correlations (both positive and negative), light pixels to low correlations). It is immediately clear that, as far as the error is concerned (top four lines), in most cases the mesh metric obtained by taking the average of the elemental metrics yields a higher correlation than the mesh metric obtained by taking the value issued by the worst element. As a consequence of this observation, we select as global mesh size parameter h the average diameter of the circumscribed circle. Remark that, as far as the condition numbers of the stiffness matrix are concerned, we observe instead a high (sometimes higher) correlation with the metrics obtained by taking the value corresponding to the "worst" element. However, the

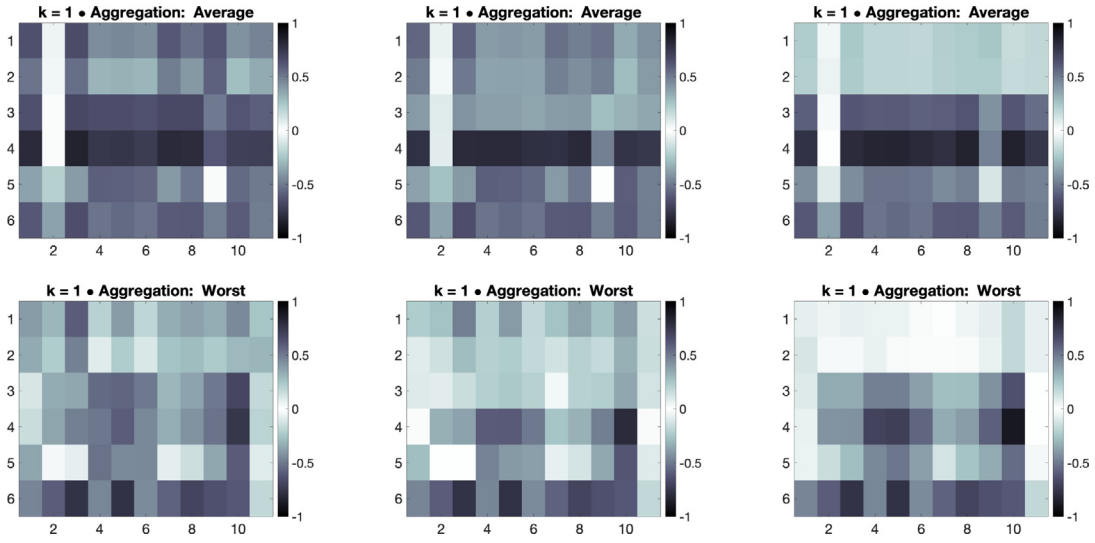

Fig. 9. Scale invariant mesh metrics (average (top) and worst (bottom) aggregation strategy) vs scaled performance indices for order $k = 1$, Test cases 1, 2 and 3 (left to right). Metrics: CR(1), KAR(2), APR(3), sSE(4), sMPD(5), ER(6), SR(7), MA(8), MX(9), NS(10), ISO(11)– Performances: $C_S^{\text{err}}(1)$, $C_\pi^{\text{err}}(2)$, $C_\infty^{\text{err}}(3)$, $C_0^{\text{err}}(4)$, $C_{\text{AN}}(5)$, $\text{Eff}_{\text{ICHOL}}(6)$. The overall darker color of the images in the top rows confirms that the performance indices have a higher correlation with the quality metrics obtained with the average aggregation strategy. (For interpretation of the references to color in this figure legend, the reader is referredto the web version of this article.).

scaled performance indicator relative to the condition number, defined as the ratio between the condition numbers of the unpreconditioned and preconditioned stiffness matrices, does not involve the mesh size parameter.

3.5. Mesh quality — solver performance correlation

Considering once again the VEM method of order $k = 1$, we now focus on the scale invariant quality metrics and scaled performance indicators. For all three test cases and both "average" and "worst" aggregation strategies, we compute the Spearman correlation index between the six scaled performance indices and the 11 scale invariant performance metrics. We report the results in Fig. 9, which is read similarly to Fig. 8 (dark pixels $\sim$ high correlation). The corresponding correlation tables are included in Appendix B, along with the scatter plots of the metric/index couples yielding the highest (in absolute value) 6 correlations. Also for the scale invariant metrics and performance indices, we observe that in general, the mesh quality metrics obtained by taking the mean of the elemental metrics have a higher correlation than the corresponding metric obtained by taking the value corresponding to the worst element. We also observe that one performance index, namely the scaled L^2 error, presents a sensibly higher correlation with the mesh metrics than most of the other performance indices. This is confirmed by the selected scatter plots in Appendix B, mostly devoted to such performance index, from which we can clearly see a qualitative dependence of the performance index (on the y axis) on the different mesh quality metrics (on the x axis). In the scatter plots, each point corresponds to a different mesh, the color/symbol code corresponding to the different mesh classes (random and the different parametric classes). The effectiveness of the incomplete Choleski preconditioner also has a high correlation with some of the mesh quality metrics, and it is the one performance index that has a higher correlation with the mesh quality metrics obtained by the "worst element" aggregation method, than with the ones resulting from averaging the elemental metrics. Remark that the effectiveness of the preconditioners is the only index independent of the test case (though, for convenience, we recompute it for each test case). We now look, for the three test cases, at the mesh metrics yielding the highest correlation with each performance index. The corresponding scatter plots are presented in Figs. 10–12. A first information is given by selection of the most correlated metric itself: over the three cases and six performance index, four metrics stand out: average maximum angle, average area/perimeter^2 ratio, worst (maximum) number of edges and worst (lowest) scaled minimum point

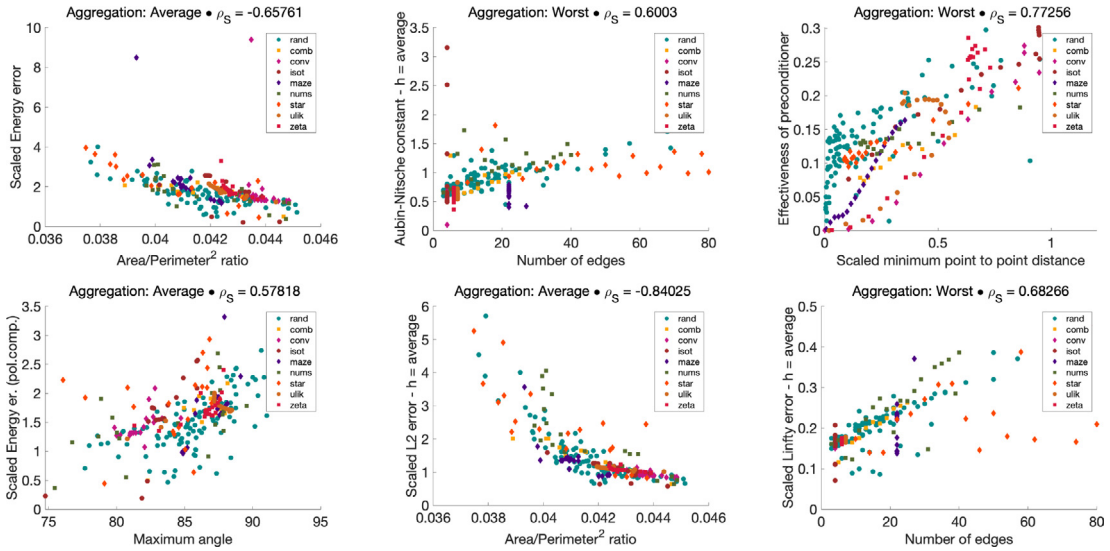

Fig. 10. Test 1, $k = 1$ — Scatter plot of the scaled performance indices vs the corresponding most correlated scale invariant metric. Each mesh is represented by the point (x, y) with x being the value of the metric and y the value of the performance. Different colors/symbols correspond to polygons in the different parametric or random classes. (For interpretation of the references to color in this figure legend, the reader is referredto the web version of this article.).

to point distance. More in detail, the two H^1-type errors (namely the energy error, and the polynomial component of the energy error), have the highest correlation with the average Area/perimeter^2 ratio and average maximum angle. The fact that the average aggregation method is the one selected, suggests that the theory, for which the energy norm error estimate is bound in terms of the maximum element size and of the constants related to the worst element, is quite pessimistic, and that few isolated "bad" elements have a limited influence on the H^1 accuracy of the method. Focusing on the scaled energy error, looking at the scatter plot depicting such a performance index vs. the average Area/Perimeter^2 ratio, we observe, for the first two test cases, a qualitatively close to linear dependence of the index on the performance metric, with the exception of few (two or three) extremely pathological grids. The outliers are two parametric meshes, namely the `convexity` and the `maze` mesh, for the worst value of the parameter (which, in both cases, is set to be equal to 1). Remark, however, that also for these outliers, the performance remains reasonably bounded (less than 50) even for the more challenging Test 3, where, however, the qualitative dependence on the most correlated mesh quality metric (the average maximum angle) is less clear. We can also observe that, with the exception of the outliers, the polynomial component of the discrete energy error (which is equal to the broken H^1 seminorm) has the same order of magnitude as the global discrete energy error. An interesting, in our opinion, observation, is also that in all the cases in which the number of edges appears as the most correlated mesh quality metric, the selected aggregation method is always the worst element value. This would suggest that even an isolated element with a high number of edges can negatively affect the performance of the method. The last observation is that, though its dependence on the mesh quality index appears more random, the scaled polynomial component of the energy error behaves extremely well in all three cases.

3.6. Geometry/performance correlation on the mirrored meshes

We now consider the scaled performance metrics evaluated on the whole set of meshes, including the mirrored meshed in D_1 and D_2. We aim at checking whether (and how) the geometrical degradation of the mesh affects the behavior of the method as the mesh is progressively refined. The scale invariant mesh quality indicators are constructed in such a way that they have the same values for the corresponding meshes in the dataset D_0, D_1 and D_2 obtained by mirroring. In turn, the scaled performance indices are also expected to be at least asymptotically and under some shape regularity constraint. In Figs. 13–15, we show the scatter plots illustrating the relation between each performance index and the quality metric that has the highest respective correlation. In these figures different

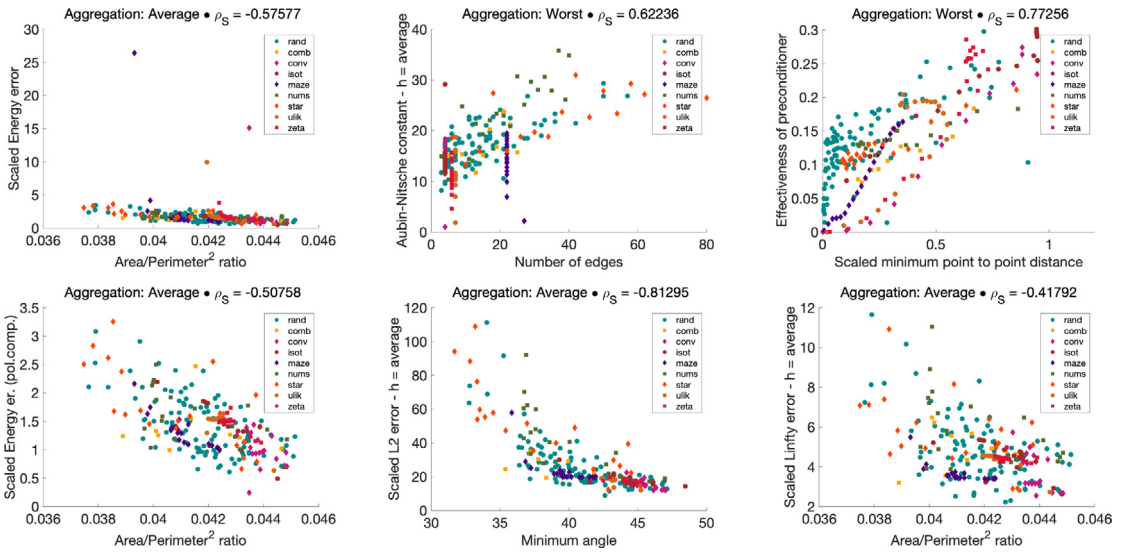

Fig. 11. Test 2, $k = 1$ — Scatter plot of the scaled performance indices vs the corresponding most correlated scale invariant metric. See the caption of Fig. 10 for more details..

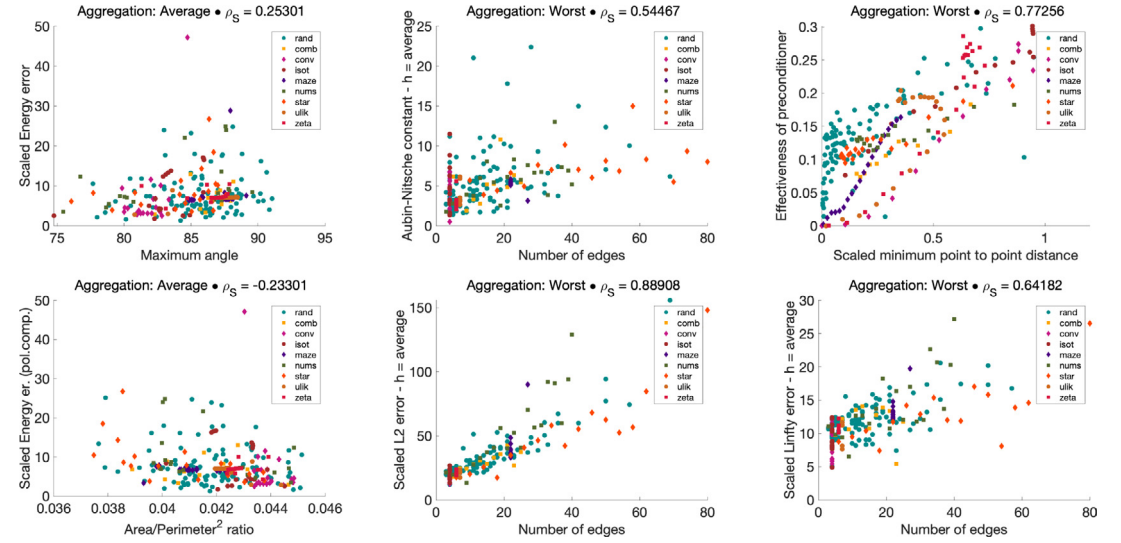

Fig. 12. Test 3, $k = 1$ — Scatter plot of the scaled performance indices vs the corresponding most correlated scale invariant metric. See the caption of Fig. 10 for more details..

color/symbols represent the three different datasets (green circle for D_0, yellow square for D_1 and crimson diamond for D_2). In most cases we observe a superposition of the point clouds relative to the three datasets, confirming the robustness of the virtual element method and the expected convergence of the method also for meshes containing very badly shaped elements and challenging test case. For the gentlest test case, namely Test 1, we even observe a sort of super convergence phenomenon, visible in the scatter plot for the two scaled energy errors (both total and polynomial component) and for the scaled L^∞ error. The L^2 error, on the other hand, scales as expected, and the result on the combined dataset confirms the high correlation with the area/perimeter^2 ratio, already observed on the sole dataset D0. Focusing on the most challenging test case, namely Test no. 3, we observe that the cloud points relative to the scaled energy error (both total and polynomial component) are overall well superposed. Conversely, the scaled L^∞ error is worse for the intermediate dataset D_1 than it is for the coarser dataset D_0 and D_2. This does

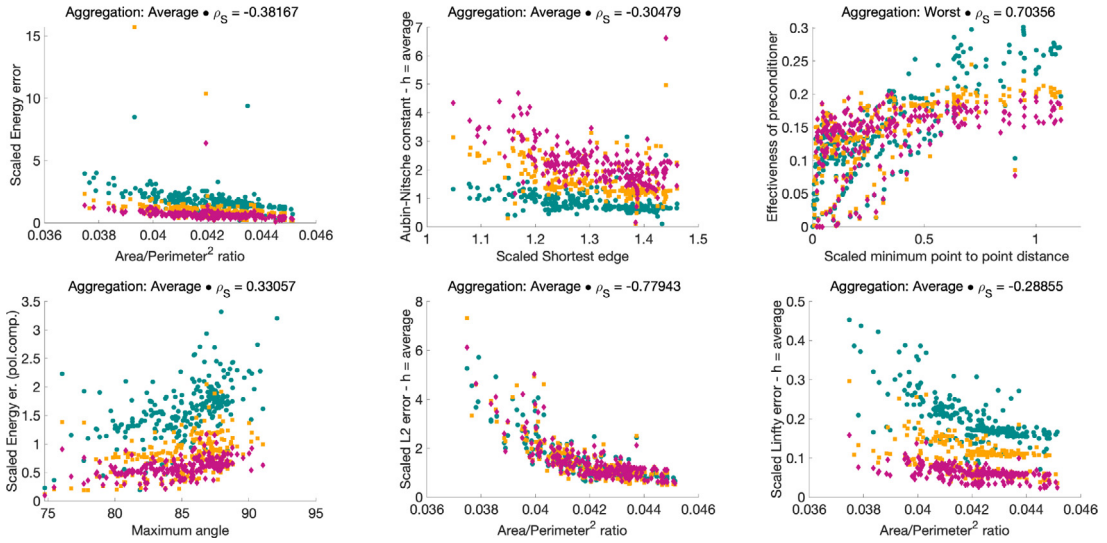

Fig. 13. Test 1, $k = 1$ — Cumulative results for datasets refined by mirroring. Scatter plot of the scaled performance indices vs the corresponding most correlated scale invariant metric. Different colors/symbols correspond to the different datasets: D_0 (green circles), D_1 (yellow squares) and D_2 (crimson diamonds). Observe the superconvergence phenomenon for the energy and L^∞ error, which appear to converge faster than h^k. (For interpretation of the references to color in this figure legend, the reader is referred to the web version of this article.)

not happen for the two other test cases, and it is probably related to the different relative positions of the "bad" elements in the meshes and of the peak of the solution (as the meshes of D_1 are the result of a 2×2 mirroring operation, one of the four polygonal elements is almost always centered at the point $(.25, .25)$ which is also the center of the peak of the solution of Test 3). We conclude by remarking that, when considering the combined three dataset, the mesh quality metrics selected are almost always the ones obtained by averaging the elemental metrics, rather than taking the value of the metric in the worst element (with the notable exception of the quality metric affecting the effectiveness of the preconditioner), strengthening the hypothesis that few isolated "bad" elements have lowest influence on the accuracy of the method than what is predicted by the theory.

3.7. Comparison between methods of different orders

We want now to gain some insight on the combined influence of geometry and order of the method on the performance of the method itself. Most theoretical results on the performance of the VEM are proven for k fixed, and they do not provide an analysis of the influence of the order of the method. Notable exceptions are [36], that however, give some (quite pessimistic, as far as the dependence in k is concerned) a priori bound only for polygonal meshes satisfying the very restrictive assumptions that the ratio between the radius of the circumscribed circle and both the ratio of the circle inscribed in the kernel and the distance of any two vertexes are lower than a constant. We limit ourselves to consider Test no. 2, whose solution is sufficiently smooth to profit from higher order discretization, while also exhibiting a sufficient variation to put the methods, defined on a relatively coarse grid, to the test. Moreover, we perform our tests on a slightly modified mesh dataset, where we agglomerate the smallest triangular element so that the resulting agglomerated polygon has a diameter of a similar size to the central polygon. Focusing on three of the scaled performance index, and on six scale independent geometric quality measures, in Figs. 16–18 we plot the superposed scatter plots for $k = 1$, 2 and 3. In these scatter plots, different colors/symbols refer to methods of different polynomial order: $k = 1$ (green circles), $k = 2$ (yellow squares) and $k = 3$ (crimson diamonds). To make the effect of the polynomial order and of the quality metric more evident, we use a semi logarithmic scale, and we plot the logarithm of the performance index against the value of the mesh quality metric. We observe that both the scaled energy error and the scaled L^2 error increase with the polynomial degree. This is to

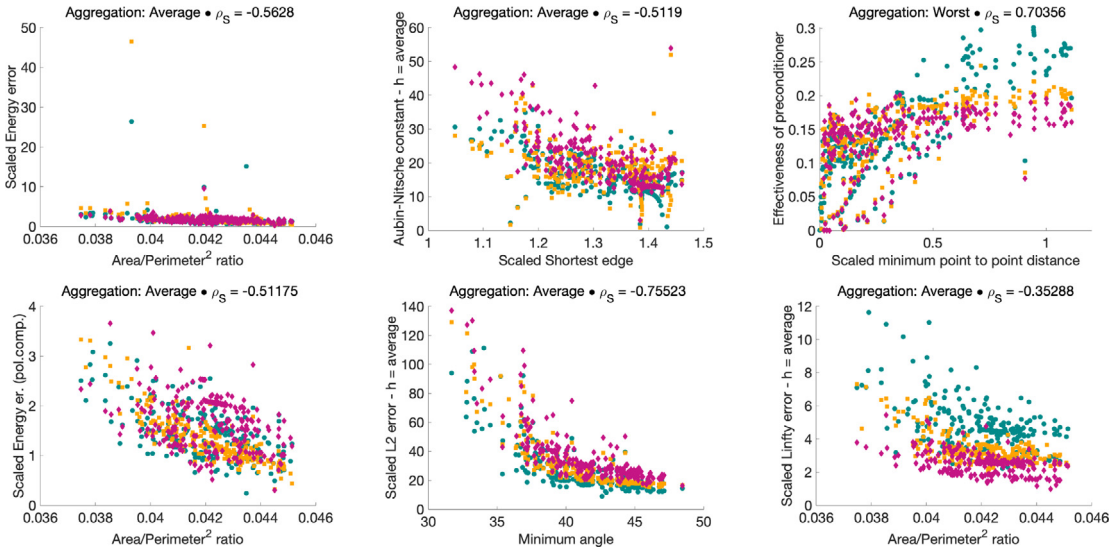

Fig. 14. Test 2, $k = 1$ — Cumulative results for datasets refined by mirroring (see Fig. 13 for more details). Here we observe that all the errors scale as expected.

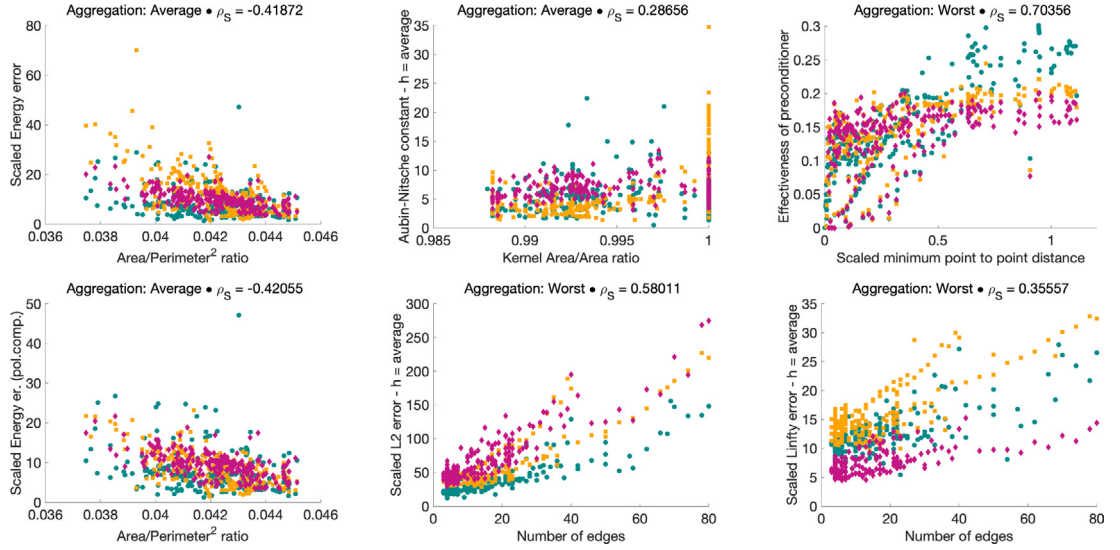

Fig. 15. Test 3, $k = 1$ — Cumulative results for datasets refined by mirroring (see Fig. 13 for more details). Due to the position of the polygonal element relative to the center of the peak, the error for the dataset D_1 (yellow squares) is worse than the one obtained with both the coarser dataset D_0 (green circles) and D_1 (crimson diamonds). (For interpretation of the references to color in this figure legend, the reader is referred to the web version of this article.)

be expected as the constants affecting the error bounds (such as, for instance, the constants C_0 and C_1 in the bound (A.3)) on the stabilization term are known to behave badly when the polynomial order of the method increases. If we consider instead the dependence of the scaled errors on the selected scale invariant mesh quality metrics, we can observe that the effect of varying the maximum angle, number of edges and kernel area/area ratio is at most very feeble, if not null. The effect of the minimum angle, inscribed/circumscribed circle ratio and area/perimeter^2 ratio is instead evident, and it is even stronger for the scaled L^2 error.

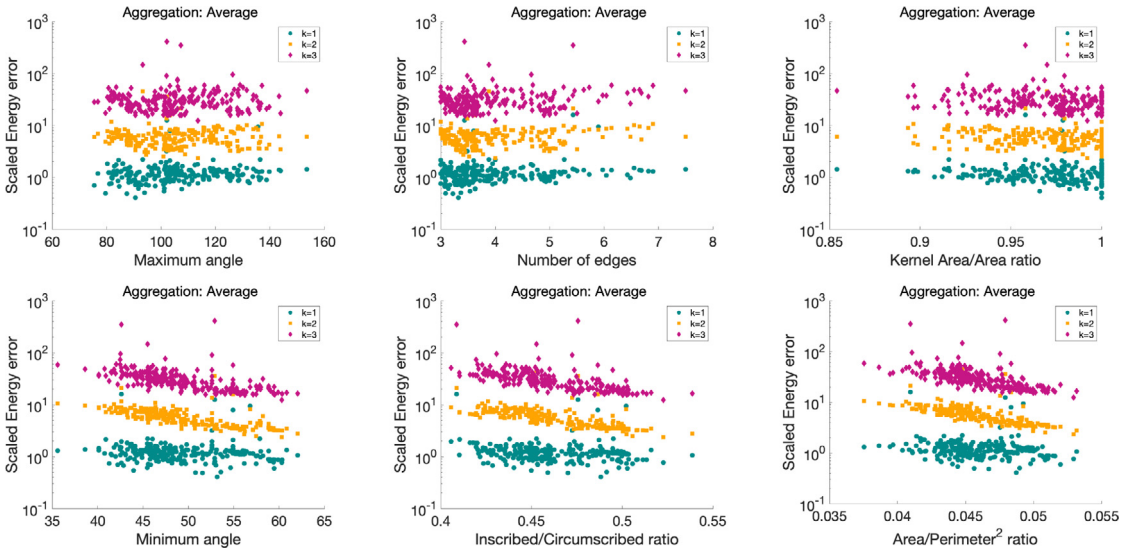

Fig. 16. Test 2 — Influence of six scale invariant metrics on the scaled energy error for methods of order $k = 1$ (green circles), $k = 2$ (yellow squares) and $k = 3$ (crimson diamonds). (For interpretation of the references to color in this figure legend, the reader is referred to the web version of this article.)

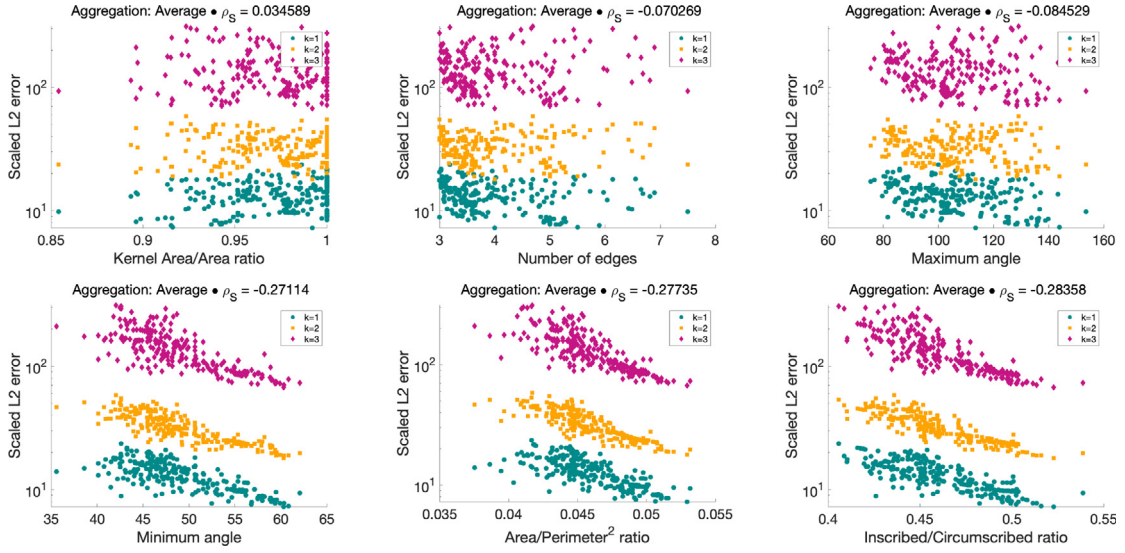

Fig. 17. Test 2 — Influence of six scale invariant metrics on the polynomial component of scaled energy error for methods of order $k = 1$ (green circles), $k = 2$ (yellow squares) and $k = 3$ (crimson diamonds). (For interpretation of the references to color in this figure legend, the reader is referred to the web version of this article.)

4. Conclusions and future work

We have presented a benchmark to study the correlation between the geometric properties of polygonal meshes, and the performances of Polytopal Element Methods (PEM) in 2D. To the best of our knowledge this is the first tool to systematically study the correlation between polygonal meshes and PEM solvers in the presence of badly shaped elements. The results obtained by testing the VEM on such a benchmark, allowed us to make some interesting observation and suggested some possible research directions relative to the theoretical analysis of the method, such as the study of the different behavior of the condition number for even and odd order methods, and of the stability and error bounds for non star shaped polygonal elements. In particular, though no single quantity seems to drive,

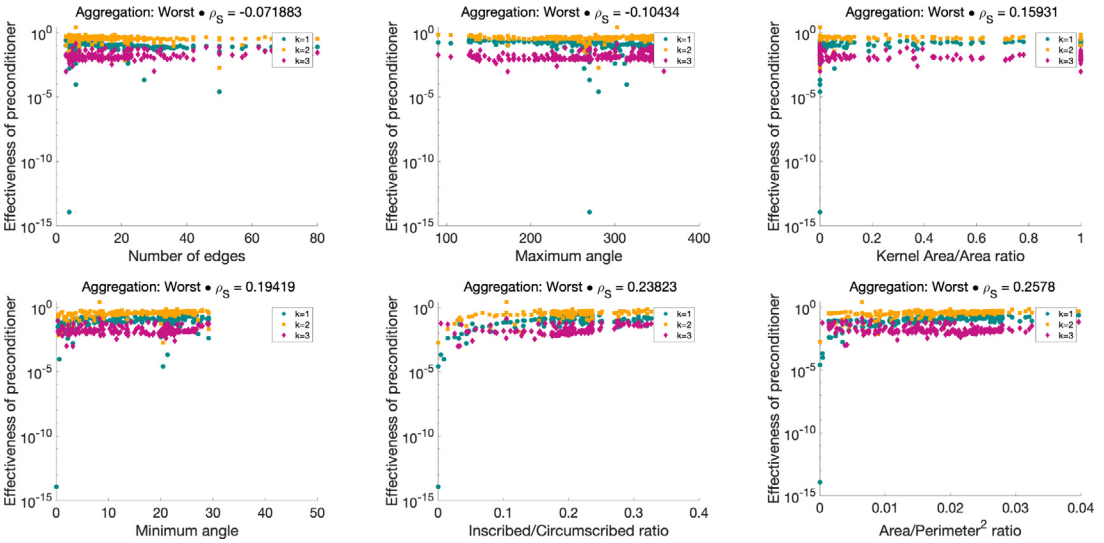

Fig. 18. Test 2 — Influence of six scale invariant metrics on the effectiveness of the ICHOL preconditioner for methods of order $k = 1$ (green circles), $k = 2$ (yellow squares) and $k = 3$ (crimson diamonds). (For interpretation of the references to color in this figure legend, the reader is referred to the web version of this article.)

by itself, the performance of the method, the role of quantities such as the area/perimeter^2 ratio or the maximum angle, that seem to play a relevant role in the accuracy of the method, needs to be better understood. We believe that not only the results obtained by such an analysis will likely carry over to similar methods (such as, for instant the non conforming VEM method and the Hybrid High Order (HHO) method), but, more importantly, that the analysis methodology itself can have an impact in understanding the role of shape regularity in the performance of polytopal methods.

Future work will focus, on the one hand, on studying the performance of other PEM solvers, such as the HHO method and the Hybridizable Discontinuous Galerkin (HDG) method. On the other hand, an interesting direction for future improvements will consist in studying the space of 2D tilings [17,18], by matching it with the concept of parametric polygons used in the benchmark. This would allow to create meshes fully made of polygons subject to study, without having to fill the canvas with triangles. Finally, we are of course interested in extending the benchmark to the volumetric case, to study the performances of PEM solvers also on general polyhedral meshes in 3D. Such extension is far from trivial though, as the number of geometric measures and associated metrics to be considered is likely to be considerably higher. At PEM level, future work will be focused mainly on the evaluation of the performance of new solvers by investigating the mutual influence of shape regularity criteria and increasing polynomial degree.

Acknowledgment

This work has been supported by the EU ERC Advanced Grant CHANGE, grant agreement No. 694515.

Appendix A. The Virtual Element Method (VEM)

We briefly recall the definition and the main properties of the order k Virtual Element Method [34], focusing on the Poisson equation

$$-\Delta u = f \text{ in } \Omega, \qquad u = 0 \text{ on } \partial\Omega, \tag{A.1}$$

where $\Omega \subset \mathbb{R}^2$ is a bounded polygonal domain, $\partial\Omega$ denotes its boundary, and $f \in L^2(\Omega)$ is a square integrable function. To this end, we consider a family $\{\mathcal{T}_h\}_h$ of tessellations of Ω into a finite number of simple polygons K, and we let $\mathcal{E}_h$ be the set of edges e of $\mathcal{T}_h$. For each polygon $K \in \mathcal{T}_h$, let the local space V^K be defined as

$$V^K = \left\{ v \in H^1(K) : v|_{\partial K} \in C^0(\partial K),\, v|_e \in \mathbb{P}_k(e)\, \forall e \in \mathcal{E}^K,\ \ \Delta v \in \mathbb{P}_{k-2}(K) \right\},$$

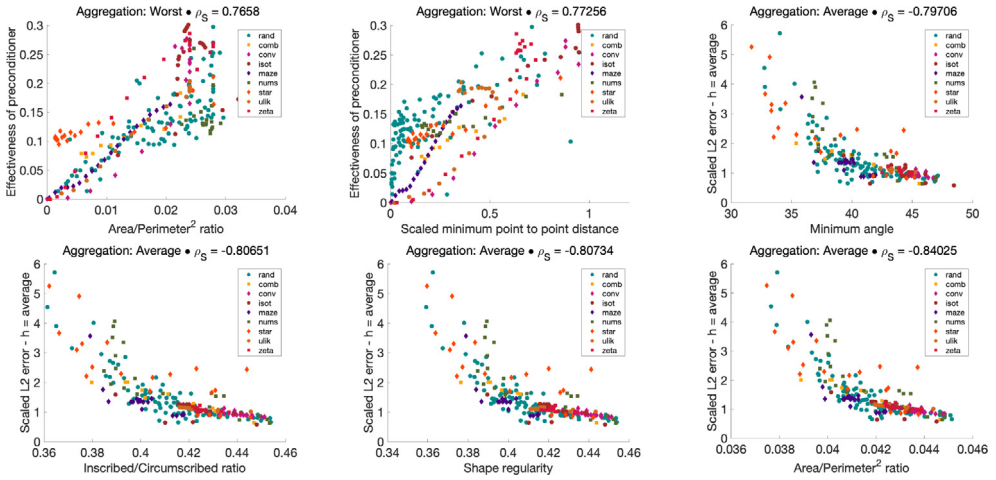

Fig. B.19. Test 1, $k = 1$ — Scatter plots corresponding to the six highest correlation index. (For interpretation of the references to color in this figure legend, the reader is referredto the web version of this article.).

where $\mathbb{P}_k(D)$ denote the restriction to D of the space of polynomials of degree less than or equal to k. The global virtual element space V_h of order k is defined as

$$V_h = \{v \in V : w|_K \in V^K \ \forall K \in \mathcal{T}_h\}.$$

Degrees of freedom, uniquely identifying a function $v_h \in V_h$, are

- the values of v_h at the vertices of the tessellation
- the values of v_h at the $k-1$ interior nodes of the $k+1$ points Gauss–Lobatto quadrature formula on each edge
- the scaled moments up to order $k-2$ of v_h in each element K.

Letting $(\cdot,\cdot)$ be the scalar product in L^2, and letting $a(u,v) = (\nabla u, \nabla v)$, solving (A.1) by a Galerkin approach, would require looking for $u_h \in V_h$ such that for all $v_h \in V_h$

$$a(u_h, v_h) = \int_\Omega f\, v_h\, dx. \tag{A.2}$$

However, evaluating both the term at the right and at the left hand side would require computing the elements of the space V^K, which implies solving PDEs in each element. The idea is then to replace both right and left hand sides with some approximation directly computable with the sole knowledge of the values of the degrees of freedom of u_h and v_h. To this aim, for each $K \in \mathcal{T}_h$, we set

$$a^K(u_h, v_h) = \int_K \nabla u_h \cdot \nabla v_h\, dx$$

and observe that, by using Green's formula, given any $v_h \in V^K$ and any $p \in \mathbb{P}_1(K) \subseteq V^K$

$$a^K(p, v_h) = \int_{\partial K} v_h \frac{\partial p}{\partial n}.$$

Since on each edge of K v_h is a known order k polynomial and $\partial p/\partial n$ is a known order $k-1$ polynomial, the right hand side can be computed exactly. This allows to define the "element by element" exactly computable projection operator $\Pi^\nabla : V^K \longrightarrow \mathbb{P}_1(K)$

$$a^K(\Pi^\nabla u_h, q) = a^K(u_h, q) \quad \forall q \in \mathbb{P}_k(K), \qquad \int_{\partial K} \Pi^\nabla u_h = \int_{\partial K} u_h.$$

We clearly have

$$a^K(u_h, v_h) = a^K(\Pi^\nabla u_h, \Pi^\nabla v_h) + a^K(u_h - \Pi^\nabla u_h, v_h - \Pi^\nabla v_h).$$

Table B.4
Test 1 — Correlation indices, average aggregation method.

	CR	KAR	APR	sSE	sMPD	ER	SR	MA	MX	NS	ISO
errS	−0.53	−0.12	−0.55	−0.35	−0.37	−0.34	−0.51	−0.44	0.49	0.33	−0.36
errπ	−0.47	−0.067	−0.49	−0.31	−0.32	−0.3	−0.46	−0.39	0.46	0.25	−0.32
errinf	−0.33	0.31	−0.34	−0.55	−0.54	−0.53	−0.34	−0.46	−0.038	0.52	−0.46
err0	−0.75	0.071	−0.78	−0.73	−0.74	−0.71	−0.75	−0.76	0.51	0.67	−0.7
AN	−0.35	−0.16	−0.37	−0.23	−0.24	−0.23	−0.36	−0.3	0.41	0.22	−0.24
Eprec	0.59	0.28	0.62	0.52	0.55	0.52	0.58	0.59	−0.43	−0.54	0.49

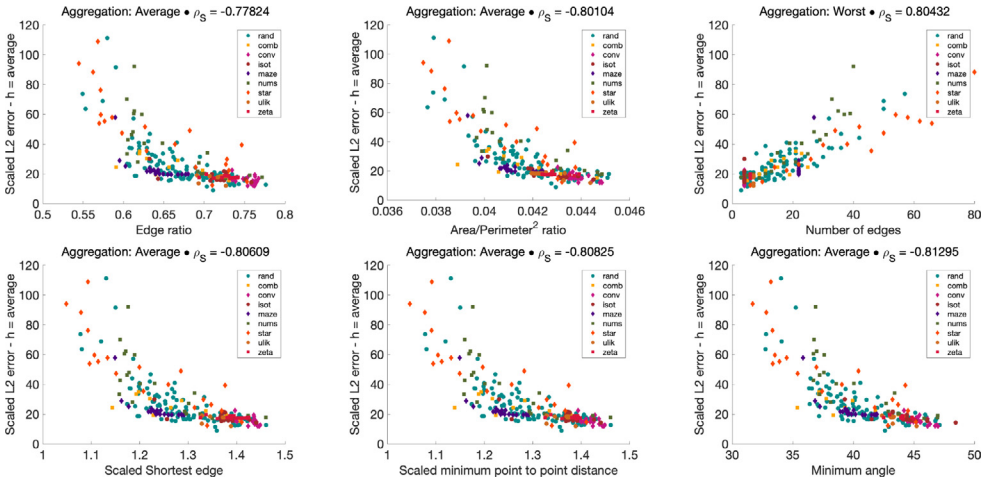

Fig. B.20. Test 2, $k = 1$ — Scatter plots corresponding to the six highest correlation index. (For interpretation of the references to color in this figure legend, the reader is referredto the web version of this article.).

The Virtual Element method stems from replacing the second term of the sum on the right hand, that cannot be computed exactly, with any computable symmetric bilinear form S satisfying for all v_h with $\Pi^\nabla v_h = 0$

$$c_0 a^K(v_h, v_h) \le S(v_h, v_h) \le c_1 a^K(v_h, v_h), \tag{A.3}$$

for two positive constants c_0 and c_1. Different recipes have been proposed in the literature for the construction of the stabilizing bilinear form S. Following the so called D-recipe, we let S be defined as a weighted Euclidean product of the vector of degrees of freedom, the weight for the degree of freedom corresponding to a basis function ϕ_i being defined as the maximum of 1 and $|\Pi^\nabla \phi_i|^2_{1,K}$ (for more details see [38]).

We then define

$$a_h^K(u, v) = a^K(\Pi^\nabla u, \Pi^\nabla v) + S(u - \Pi^\nabla u, v - \Pi^\nabla v).$$

Additionally, letting $\Pi_k^0 : L^2(K) \to \mathbb{P}_{k-2}(K)$ denote the $L^2(K)$ orthogonal projection onto the space of polynomials of order up to k, we let $f_h^K = \Pi_{k-2}^0 f$.

The virtual element discretization of (A.2) yields the following discrete problem:

Problem A.1. Find $u_h \in V_h$ such that

$$a_h(u_h, v_h) = f_h(v_h) \qquad \forall v_h \in V_h$$

with $a_h(u_h, v_h) = \sum_K a_h^K(u_h, v_h)$ and $f_h(v_h) = \sum_K \int_K f_h^K v_h$.

Problem A.1 is usually analyzed under the following assumption on the polygons of the tessellation.

Assumption A.2. There exist constants $\gamma_0, \gamma_1 > 0$ such that

(i) each element $K \in \mathcal{T}_h$ is star-shaped with respect to a ball of radius $\ge \gamma_0 h_K$, where h_K is the diameter of K;

Table B.5
Test 1 — Correlation indices, worst element aggregation method.

	CR	KAR	APR	sSE	sMPD	ER	SR	MA	MX	NS	ISO
errS	−0.32	−0.31	−0.53	−0.1	−0.34	−0.12	−0.31	−0.34	0.33	0.34	−0.18
errπ	−0.24	−0.23	−0.38	−0.073	−0.22	−0.1	−0.25	−0.25	0.26	0.25	−0.22
errinf	0.37	0.051	0.079	−0.49	−0.37	−0.38	0.14	−0.018	0.24	0.57	0.19
err0	−0.099	−0.28	−0.43	−0.44	−0.54	−0.38	−0.24	−0.32	0.46	0.71	−0.092
AN	−0.2	−0.28	−0.29	−0.07	−0.22	−0.096	−0.25	−0.22	0.3	0.22	−0.19
Eprec	0.39	0.46	0.68	0.45	0.75	0.43	0.45	0.64	−0.56	−0.58	0.13

Table B.6
Test 2, $k-1$ — Average aggregation method.

	CR	KAR	APR	sSE	sMPD	ER	SR	MA	MX	NS	ISO
errS	−0.72	−0.29	−0.75	−0.57	−0.59	−0.57	−0.72	−0.69	0.57	0.62	−0.58
errπ	−0.82	−0.12	−0.84	−0.7	−0.72	−0.7	−0.81	−0.79	0.61	0.69	−0.71
errinf	−0.065	0.58	−0.053	−0.3	−0.28	−0.27	−0.057	−0.16	−0.25	0.19	−0.23
err0	−0.87	0.042	−0.89	−0.9	−0.91	−0.88	−0.87	−0.91	0.51	0.85	−0.85
AN	−0.57	0.063	−0.57	−0.51	−0.52	−0.5	−0.55	−0.55	0.41	0.51	−0.52
Eprec	0.59	0.28	0.62	0.52	0.55	0.52	0.58	0.59	−0.43	−0.54	0.49

Table B.7
Test 2, $k=1$ — Worst element aggregation method.

	CR	KAR	APR	sSE	sMPD	ER	SR	MA	MX	NS	ISO
errS	−0.27	−0.56	−0.72	−0.37	−0.63	−0.31	−0.52	−0.56	0.55	0.65	−0.021
errπ	−0.16	−0.47	−0.59	−0.47	−0.6	−0.38	−0.43	−0.43	0.5	0.73	0.011
errinf	0.39	0.46	0.36	−0.2	−0.032	−0.096	0.49	0.25	−0.14	0.23	0.11
err0	−0.042	−0.38	−0.44	−0.69	−0.72	−0.57	−0.32	−0.38	0.55	0.89	0.023
AN	−0.074	−0.17	−0.38	−0.17	−0.31	−0.1	−0.12	−0.22	0.22	0.56	0.034
Eprec	0.39	0.46	0.68	0.45	0.75	0.43	0.45	0.64	−0.56	−0.58	0.13

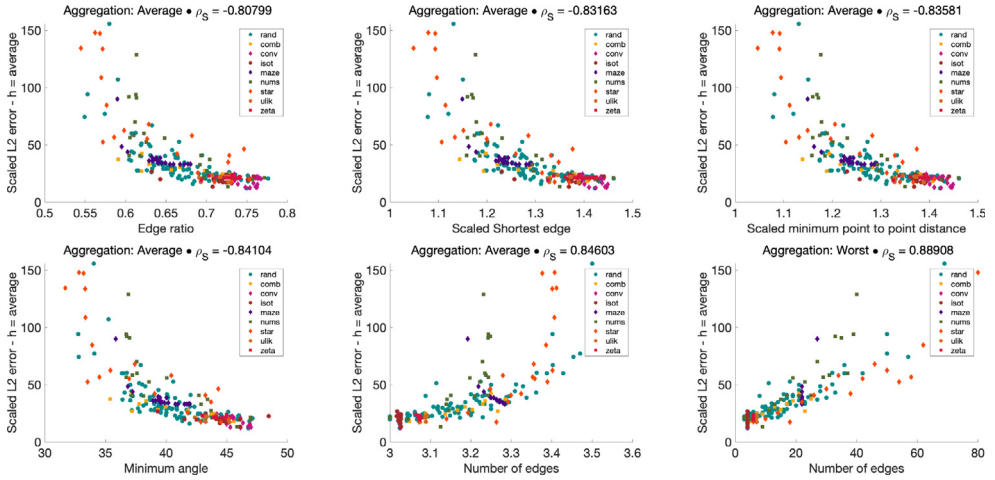

Fig. B.21. Test 3, $k=1$ — Scatter plots corresponding to the six highest correlation index. (For interpretation of the references to color in this figure legend, the reader is referredto the web version of this article.).

(ii) for each element K in $\mathcal{T}_h$ the distance between any two vertices of K is $\geq \gamma_1 h_K$.

Under this assumption, stability and optimal order one convergence are proven for different choices for the bilinear form S (see [38]), including the simple one (which we used in the numerical tests) mentioned above. For

Table B.8
Test 3, $k-1$ — Correlation indices, average aggregation method.

	CR	KAR	APR	sSE	sMPD	ER	SR	MA	MX	NS	ISO
errS	−0.57	−0.4	−0.6	−0.46	−0.49	−0.47	−0.59	−0.58	0.44	0.58	−0.46
errπ	−0.59	−0.24	−0.62	−0.58	−0.58	−0.58	−0.63	−0.64	0.41	0.65	−0.56
errinf	0.18	0.58	0.21	0.056	0.08	0.082	0.21	0.18	−0.28	−0.2	0.065
err0	−0.65	0.13	−0.66	−0.63	−0.64	−0.62	−0.63	−0.66	0.41	0.6	−0.61
AN	−0.48	0.11	−0.48	−0.46	−0.47	−0.43	−0.46	−0.47	0.31	0.49	−0.44
Eprec	0.59	0.28	0.62	0.52	0.55	0.52	0.58	0.59	−0.43	−0.54	0.49

Table B.9
Test 3, $k=1$ — Correlation indices, worst element aggregation method.

	CR	KAR	APR	sSE	sMPD	ER	SR	MA	MX	NS	ISO
errS	−0.26	−0.65	−0.74	−0.37	−0.64	−0.38	−0.58	−0.55	0.66	0.57	0.014
errπ	−0.075	−0.56	−0.54	−0.49	−0.58	−0.48	−0.48	−0.38	0.64	0.63	0.078
errinf	0.38	0.64	0.52	0.23	0.42	0.27	0.61	0.43	−0.47	−0.16	0.021
err0	0.0049	−0.18	−0.32	−0.37	−0.42	−0.31	−0.12	−0.24	0.3	0.66	−0.022
AN	0.0029	−0.095	−0.3	−0.12	−0.21	−0.037	−0.019	−0.095	0.11	0.54	0.16
Eprec	0.39	0.46	0.68	0.45	0.75	0.43	0.45	0.64	−0.56	−0.58	0.13

details on the implementation as well as for the study of the convergence, stability and robustness properties of the method we refer to [34,35].

Under Assumption A.2, it is possible to prove that the discrete

$$\|u-u_h\|_{1,\Omega} \leq Ch^k \|u\|_{k+1,\Omega}. \tag{A.4}$$

Care is needed when computing the relative errors ϵ_∞ and ϵ_2 for VEM. Since the analytic expression of a VEM function is not known, we can only use its degrees of freedom and all the information we can deduce from them. In particular, for the lowest order VEM, the degrees of freedom are the pointwise values at the mesh vertices $\mathcal{P} = \{\mathbf{p}_i\}_i$, $i = 1, \ldots, N_{\text{vertices}}$. Thus, to compute ϵ_∞ and ϵ_2, we define $\|u-u_h\|_\infty := \max_i |u(\mathbf{p}_i) - u_h(\mathbf{p}_i)|$, and replace $\|u-u_h\|_2$ with $\|u - \Pi^\nabla u_h\|$.

Appendix B. Scatterplot corresponding to the highest correlation index

See Figs. B.19–B.21 and Tables B.4–B.9.

References

[1] P.F. Antonietti, A. Cangiani, J. Collis, Z. Dong, E.H. Georgoulis, S. Giani, P. Houston, Review of discontinuous Galerkin finite element methods for partial differential equations on complicated domains, in: Connections and Challenges in Modern Approaches To Numerical Partial Differential Equations, Springer, 2016, pp. 279–308.

[2] J. Brandts, S. Korotov, M. Křížek, On the equivalence of regularity criteria for triangular and tetrahedral finite element partitions, Comput. Math. Appl. 55 (10) (2008) 2227–2233.

[3] F. Brezzi, K. Lipnikov, M. Shashkov, Convergence of mimetic finite difference methods for diffusion problems on polyhedral meshes, SIAM J. Numer. Anal. 43 (2005) 1872–1896.

[4] A. Cangiani, E.H. Georgoulis, P. Houston, hp-version discontinuous Galerkin methods on polygonal and polyhedral meshes, Math. Models Methods Appl. Sci. 24 (10) (2014) 2009–2041.

[5] P. Ciarlet, The Finite Element Method for Elliptic Problems, Society for Industrial and Applied Mathematics, 2002.

[6] B. Cockburn, B. Dong, J. Guzmán, A superconvergent LDG-hybridizable Galerkin method for second-order elliptic problems, Math. Comp. 77 (264) (2008) 1887–1916.

[7] M. Desbrun, M. Meyer, P. Schröder, A.H. Barr, Implicit fairing of irregular meshes using diffusion and curvature flow, in: Proceedings of the 26th annual conference on Computer graphics and interactive techniques, Citeseer, 1999, pp. 317–324.

[8] Y. Dodge, The Concise Encyclopedia of Statistics, third ed., Springer New York, 2008.

[9] Q. Du, V. Faber, M. Gunzburger, Centroidal voronoi tessellations: Applications and algorithms, SIAM Rev. 41 (4) (1999) 637–676.

[10] M.S. Floater, K. Hormann, Surface parameterization: a tutorial and survey, in: Advances in Multiresolution for Geometric Modelling, Springer, 2005, pp. 157–186.

[11] R. Franke, A critical comparison of some methods for interpolation of scattered data, 1979.

[12] X. Gao, J. Huang, K. Xu, Z. Pan, Z. Deng, G. Chen, Evaluating hex-mesh quality metrics via correlation analysis, Comput. Graph. Forum 36 (5) (2017) 105–116.
[13] A. Gillette, A. Rand, Shape Quality for Generalized Baricentric Interpolation, CRC Press, Taylor & Francis Group, 2018, pp. 23–42 (Ch. 2).
[14] G.H. Golub, C.F. Va. Loan, Matrix Computations, third ed., The Johns Hopkins University Press, 1996.
[15] P. Herholz, F. Haase, M. Alexa, Diffusion diagrams: Voronoi cells and centroids from diffusion, Comput. Graph. Forum 36 (2) (2017) 163–175.
[16] T.J. Hughes, J.A. Cottrell, Y. Bazilevs, Isogeometric analysis: Cad, finite elements, nurbs, exact geometry and mesh refinement, Comput. Methods Appl. Mech. Engrg. 194 (39–41) (2005) 4135–4195.
[17] C.S. Kaplan, D.H. Salesin, Escherization, in: Proceedings of the 27th Annual Conference on Computer Graphics and Interactive Techniques, ACM Press/Addison-Wesley Publishing Co, 2000, pp. 499–510.
[18] C. Kaplan, D. Salesin, Dihedral. escherization, Dihedral escherization, in: Proceedings of Graphics Interface 2004, GI 2004, Canadian Human-Computer Communications Society, School of Computer Science, University of Waterloo, Waterloo, Ontario, Canada, 2004, pp. 255–262.
[19] K. Lipnikov, On shape-regularity of polyhedral meshes for solving pdes, in: Research Notes, 22nd International Meshing Roundtable, 2013.
[20] M. Livesu, cinolib: a generic programming header only C++ library for processing polygonal and polyhedral meshes, Trans. Comput. Sci. XXXIV.
[21] M. Livesu, A heat flow relaxation scheme for n dimensional discrete hyper surfaces, Comput. Graph. 71 (2018) 124–131, http://dx.doi.org/10.1016/j.cag.2018.01.004.
[22] L. Mu, X. Wang, Y. Wang, Shape regularity conditions for polygonal/polyhedral meshes, exemplified in a discontinuous Galerkin discretization, Numer. Methods Partial Differential Equations 31 (1) (2015) 308–325.
[23] G. Patané, Star-Laplacian spectral kernels and distances for geometry processing and shape analysis, Comput. Graph. Forum 35 (2) (2016) 599–624.
[24] D.A.D. Pietro, A. Ern, Hybrid high-order methods for variable-diffusion problems on general meshes, C. R. Math. 353 (1) (2015) 31–34.
[25] D.S. Rjasanow, S. Weiß er, Higher order BEM-based FEM on polygonal meshes, SIAM J. Numer. Anal. 241 (2013) 103–115.
[26] T. Schneider, J. Dumas, X. Gao, M. Botsch, D. Panozzo, D. Zorin, Poly-spline finite element method, ACM Trans. Graph.
[27] T. Schneider, Y. Hu, J. Dumas, X. Gao, D. Panozzo, D. Zorin, Decoupling simulation accuracy from mesh quality, in: SIGGRAPH Asia 2018 Technical Papers, ACM, 2018, p. 280.
[28] J.R. Shewchuk, Triangle: Engineering a 2d quality mesh generator and delaunay triangulator, in: Applied Computational Geometry Towards Geometric Engineering, Springer, 1996, pp. 203–222.
[29] J.R. Shewchuk, What Is a Good Linear Finite Element? Interpolation, Conditioning, Anisotropy, and Quality Measures, Vol. 73, University of California at Berkeley, 2002, p. 137, (preprint).
[30] L. Simonson, G. Suto, Geometry Template Library for Stl-Like 2d Operations, Colorado, GTL Boostcon.
[31] C. Stimpson, C. Ernst, P. Knupp, P. Pébay, D. Thompson, The verdict library reference manual, Sandia National Laboratories Technical Report 9.
[32] N. Sukumar, A. Tabarraei, Conforming polygonal finite elements, Internat. J. Numer. Methods Engrg. 61 (12) (2004) 2045–2066.
[33] The CGAL Project, CGAL User and Reference Manual, 4.13 Edition, CGAL Editorial Board, 2018, URL https://doc.cgal.org/4.13/Manual/packages.html.
[34] L. Beirão da Veiga, F. Brezzi, A. Cangiani, G. Manzini, L.D. Marini, A. Russo, Basic principles of virtual element methods, Math. Models Methods Appl. Sci. 23 (1) (2013) 199–214.
[35] L. Beirão da Veiga, F. Brezzi, L.D. Marini, A. Russo, The Hitchhiker's guide to the virtual element method, Math. Models Methods Appl. Sci. 24 (08) (2014) 1541–1573.
[36] L. Beirão da Veiga, A. Chernov, L. Mascotto, A. Russo, Basic principles of hp virtual elements on quasiuniform meshes, Math. Models Methods Appl. Sci. 26 (08) (2016) 1567–1598.
[37] L. Beirão da Veiga, K. Lipnikov, G. Manzini, The Mimetic Finite Difference Method for Elliptic Problems, (11) MS&A, Springer, 2014.
[38] L. Beir ao da Veiga, L.C.A. Russo, Stability analysis for the virtual element method, Math. Models Methods Appl. Sci. 27 (13) (2017) 2557–2594.
[39] J. Wang, X. Ye, A weak Galerkin finite element method for second-order elliptic problems, J. Comput. Appl. Math. 241 (2013) 103–115.
[40] S. Weisser, Anisotropic Polygonal and Polyedral Discretizations in Finite Element Analysis, Vol. 53, 2019, pp. 475–501.
[41] E. Welzl, Smallest enclosing disks (balls and ellipsoids), in: New Results and New Trends in Computer Science, Springer, 1991, pp. 359–370.